Nickel isotope fractionation in komatiites and associated sulfides in the hart deposit, Late Archean Abitibi Greenstone Belt, Canada

R.S. Hiebert, A. Bekker, M.G. Houlé, Olivier Rouxel

Chemical Geology
August 2022, Volume 603, Pages 120912 (13p.)
https://doi.org/10.1016/j.chemgeo.2022.120912
https://archimer.ifremer.fr/doc/00771/88266/

Nickel isotope fractionation in komatiites and associated sulfides in the hart deposit, Late Archean Abitibi Greenstone Belt, Canada

Hiebert R.S. [1, *], Bekker A. [1, 2, 3], Houlé M.G. [4], Rouxel Olivier [5]

[1] Department of Geological Sciences, University of Manitoba, Winnipeg, MB R3T 2N2, Canada
[2] Department of Earth and Planetary Sciences, University of California, Riverside, CA 92521, USA
[3] Department of Geology, University of Johannesburg, Auckland Park, Johannesburg 2006, South Africa
[4] Geological Survey of Canada, Lands and Minerals Sector, Natural Resources Canada, Québec, QC G1K 9A9, Canada
[5] IFREMER, Centre de Brest, Unité Géosciences Marines, F-29280 Plouzané, France

* Corresponding author : R. S. Hiebert, email address : russel.hiebert@umanitoba.ca

Abstract :

Extremely light and highly variable δ60Ni values have been observed in komatiite-associated magmatic sulfides in recent studies. In this study, we examine the mechanisms of Ni isotope fractionation between silicate and sulfide liquids in the Hart komatiite-associated Fe-Ni-Cu-sulfide system. We assess the petrogenetic significance of these mechanisms using Ni isotope and concentration data. The concentration of Ni in bulk rock varies from 774 to 2690 ppm in komatiite samples with no sulfide minerals to 8380–39,300 ppm in samples almost entirely consisting of sulfide minerals. The δ60Ni values vary from +0.14‰ in komatiite samples with no sulfide minerals to −1.06‰ in samples dominantly consisting of sulfide minerals. A theoretical model of fractionation between the komatiitic lava and sulfide xenomelt with nickel isotope exchange followed by fractional crystallization during crystallization of the sulfide melt can produce a range of δ60Ni values from +0.17‰ to −1.02‰ in sulfide-rich rocks depending on the extent of fractional crystallization and the amount of trapped melt between the sulfide mineral grains, which corresponds well with the range of values observed in these rocks. This proposed model requires fractionation of Ni isotopes between sulfide liquid and the earliest formed sulfide crystals during crystallization. Effects of later crystallization during peritectic reactions and subsolidus exsolution could be tested by in situ measurements of Ni isotopes in different textural varieties of pentlandite that formed over a large range of temperatures during cooling.

Highlights

► Large Ni isotopic fractionation with unknown cause has been observed in komatiites. ► Fractionation occurs in two stages. ► Fractionation during isotopic exchange between komatiite and sulfide liquids. ► Rayleigh fractionation during crystallization of sulfide liquid.

Keywords : Nickel, Stable isotope, Komatiite, Nickel isotope

1 Introduction

It is generally accepted that during the formation of magmatic nickel sulfide deposits associated with komatiitic flows and intrusions, nickel derived from the mantle with ultramafic magmas and sulfur, typically being derived from an external source, forming an initial sulfide xenomelt (e.g. Huppert et al., 1984; Lesher et al. 1984; Lesher and Groves, 1986; Lesher 1989; Lesher and Campbell, 1993; Lesher and Burnham, 2001; Ripley and Li 2013; Lesher 2017). This melt then undergoes elemental and isotopic exchange to equilibrate with the silicate magma during which nickel, along with copper, platinum-group elements, and other chalcophile elements, are preferentially partitioned into the sulfide melt from the silicate magma (e.g. Duke and Naldrett, 1978; Duke, 1979; Lesher and Campbell 1993; Lesher and Burnham 2001; Mansur et al. 2021). During this partitioning, there is the potential for fractionation of isotopes of these metals between silicate magma and sulfide melt, although, based on thermodynamic considerations, the isotopic fractionation during this partitioning is typically considered to be insignificant due to the high temperatures involved and the small relative mass difference between isotopes of these transition metals (e.g., Urey 1947). Although the impact on Ni isotopes is not well constrained, the possible effect of partial melting and sulfide segregation on the isotopic

composition of Cu in komatiites has been investigated by Savage et al. (2015). The results demonstrated that there is limited Cu isotope fractionation during mantle melting, with silicate magma and sulfide melt differing by up to few tenths of per mil. Small Zn isotope fractionation (< 0.1‰) may also result from crystallization of isotopically light olivines and Fe-Ti-oxides at the very end of the differentiation sequence (Chen et al., 2013).

The case for Ni isotopes is more complex, and fractionations have been previously thought to be small and restricted to continental weathering (Cameron and Vance 2014; Ratié et al. 2015) or biological processes such as methanogenesis (Cameron et al. 2009). While no significant Ni isotope fractionation has been reported due to fractional crystallization or partial melting (Saunders et al., 2020), unusual and relatively large Ni isotopic fractionations up to 0.90‰ have been found between silicates and sulfides in komatiitic systems (Gueguen et al. 2013; Hofmann et al. 2014) and sulfides hosted in mafic systems such as Norilsk, Russia ($\delta^{62/60}$Ni from -1.33 ‰ to +0.63 ‰; Sergeev et al. 2019) and Sudbury (δ^{60}Ni from -1.69 ‰ to +0.41 ‰; Christoffersen 2017). Sulfide metasomatism has also been proposed to explain lighter Ni isotopic compositions in some peridotite xenoliths (Klaver et al., 2020). In addition, Ni isotopic composition of mineral separates from mantle peridotite xenoliths revealed variations up to 2.87‰, albeit most of the variations are generally within a range of 0.4‰ (Gall et al. 2017). The cause of fractionation between silicate and sulfide melts remains uncertain, but theoretical calculations have shown that Ni isotope fractionation among sulfides have an approximately linear dependence on the Ni-S bond length, temperature, and Fe/Ni ratio of sulfide minerals (Liu et al. 2018).

In this study, we analyzed the Ni isotopic composition of samples from the Hart komatiite-associated Ni-sulfide deposit to evaluate the processes responsible for the large observed Ni

isotopic fractionations in komatiitic systems and the potential petrological significance of these processes. This contribution is part of a larger project focussed on the Hart deposit that included examination of the sources of sulfur for this Ni-Cu-(PGE) deposit through the characterization of multiple sulfur and iron isotopes of the sulfides, associated komatiites and adjacent footwall lithologies (Hiebert et al. 2016), and the evaluation of the environmental conditions of deposition based on the chemical composition and multiple sulfur and iron isotopic characteristics of sedimentary rocks that acted as sulfur sources for the formation of the Hart deposit (Hiebert et al. 2018). Despite the slightly higher metamorphic grade at the Hart deposit in comparison to other deposits in the Abitibi greenstone belt, such as Alexo (e.g., Barnes and Naldrett, 1987; Houlé et al., 2012), which experienced lower to subgreenschist facies metamorphism, versus mid to upper greenschist facies at Hart (Thompson, 2005), the selection of the Hart deposit as a study area allowed us to create a more detailed isotopic characterization at the scale of a single deposit in the Abitibi. At the time of this study, exploration activity at the Hart deposit was active with the excavation of trenched exposures and abundant drill core that were available to assess the vertical and lateral variability around the deposit whereas the spectacular stripped exposure at Alexo studied by Houlé et al. (2012) were destroyed during the mining operation and drill cores were no longer available to study the vertical and lateral variation. Additionally, the presence of the exhalite and graphitic argillite that directly underlie the host komatiite unit at Hart, but are completely eroded within the ore-localizing embayment, provide a clear link between potential source rocks and a typical ore profile with massive sulfides at the base, overlain by net-textured and disseminated sulfides (Houlé et al., 2010b; Hiebert et al. 2016). These classic relationships between the host komatiite

and potential sulfur source(s) were not documented at Alexo, making such study more difficult to undertake.

2 Background geology

Numerous komatiite successions in the Late Archean Abitibi greenstone belt are well exposed and preserved (Barnes and Naldrett 1987; Houlé and Lesher 2011; Hiebert et al., 2016), including well-studied examples at Pyke Hill (Pyke et al. 1973; Houlé et al. 2009), Dundonald Beach (Houlé et al. 2008), and at classic komatiite-associated Ni-Cu-(PGE) deposit localities such as Alexo (Houlé et al. 2012) and Hart (Hiebert et al., 2013, 2018). The Abitibi greenstone belt has been tectonostratigraphically subdivided into seven volcanic and sedimentary assemblages (e.g. Thurston et al. 2008), four of which contain the majority of the komatiites (Houlé and Lesher 2011).

In the Shaw Dome, which hosts the Hart deposit, the volcano-sedimentary stratigraphy is composed of, from oldest to youngest (Fig. 1): 1) massive and pillowed intermediate volcanic rocks with lesser volumes of massive and volcaniclastic felsic volcanic rocks and thin, but laterally extensive, iron formations of the 2734–2724 Ma Deloro volcanic episode; 2) felsic to intermediate volcaniclastic rocks intruded by komatiitic dikes and sills, and intercalated with komatiitic lavas and less extensive iron formations of the lower part of the 2710 – 2704 Ma Tisdale volcanic episode; 3) komatiitic and tholeiitic mafic volcanic rocks of the middle part of the Tisdale volcanic episode; and 4) calc-alkaline felsic to intermediate volcanic rocks in the upper part of the Tisdale volcanic episode (Houlé et al. 2010a, b; Houlé and Lesher 2011).

The Hart deposit consists of two mineralized zones. The main zone is located at the base of the lowermost komatiite flow of the middle Tisdale volcanic assemblage, within a large embayment where several stacked komatiite flows overlie and crosscut the felsic to intermediate volcanic succession of the lower Tisdale assemblage and associated sedimentary rocks (Fig. 2).

Several komatiite flows were examined and sampled in drill core with boundaries between flows being identified by flow-top breccias, or, where the flow-top breccias have been removed via erosion by subsequent flows, zones of spinifex-textured rock (Fig. 3). It is, however, possible that some flow boundaries were not recognized where the spinifex zones were eroded away by overlying flows. We use barren komatiite for samples containing trace to no visible sulfide and classify sulfide-bearing komatiites based on their sulfide mineral abundance into <10%, 10-30%, 30-70%, and >70% groups. The Hart deposit consists of massive sulfides overlain by semi-massive (locally net-textured) to disseminated sulfides in komatiite (Fig. 4; Houlé et al. 2010a, b; Houlé and Lesher 2011; Hiebert et al. 2016). The eastern extension zone of the Hart deposit is hosted 12–25 m above the base of the second komatiite flow in this succession, and consists of predominantly semi-massive sulfides with lesser amounts of massive and disseminated sulfides (Hiebert et al. 2016). A third komatiite flow was sampled (H07-33-128.3) to represent komatiite that is least affected by contamination from the footwall lithologies based on trace element ratios, such as La/Nb and Zr/Ti, and S- and Fe-isotopic indicators of contamination (Hiebert et al. 2016). Sulfide mineralization in this area is predominantly pyrrhotite and pentlandite, with minor chalcopyrite (Fig. 4; Hiebert et al. 2016).

Komatiites in the study area have been metamorphosed and typically have a metamorphic silicate mineral assemblage of antigorite, tremolite, and chlorite (Fig. 5; Table 1). Typical

samples contain well preserved pseudomorphs of original olivine cumulate and spinifex textures (Fig 5a; Hiebert et al. 2016), although the preservation of primary textures degrades with increasing intensity of alteration or proximity to later intrusions (Fig 5b). Pyroxenitic komatiite containing pyroxene spinifex, was also observed in parts of drill holes H07-33 and H11-05 (Fig. 3), but no samples were included in this study. Typical barren komatiite samples are dominated by antigorite, chlorite, tremolite and chlorite (Figs. 5c and 5d). Locally, growth of metamorphic and alteration minerals obscure primary igneous textures, and the mineral assemblage contains a greater proportion of tremolite and rare, very small (<0.1 mm) metamorphic olivine formed at the expense of antigorite and other minerals. The metamorphic olivine could have formed by the breakdown of brucite and antigorite under mid- to upper-greenschist facies conditions, as has been identified elsewhere in the Abitibi greenstone belt (Jolly 1982; Arndt et al., 2008), possibly indicating locally developed higher temperature conditions related to later igneous activity.

In the southern and eastern areas of the study area (drill holes H07-33, H11-11 and H11-13C), carbonate alteration is also present as small (<0.05 mm) stringers in slightly altered komatiitic samples that maintain well-preserved primary textures. In samples of stronger carbonatization, carbonate grains occur as discrete rhombohedrally shaped carbonate crystals (likely magnesite; 0.1 – 0.5 mm; Figs. 4a, 5b, 5g and 5h). Veinlets of carbonate are thin (≤0.1 mm) and rare. In drill hole H11-13C, carbonate altered samples are in close proximity to later granitic porphyry intrusions and might be related to these intrusions, although this has yet to be established.

3 Analytical methods

Samples for this study were selected from several diamond drill cores located along three local grid sections (Figs. 2 and 3; Table 2). Samples were selected to be representative of different sulfide abundances and non-mineralized komatiite. The Ni isotope analyses were completed at the Pôle Spectrométre Océan (PSO) located at IFREMER (Brest, France) following the method described in Gueguen et al. (2013) and summarized here. Sample materials were dissolved in double-distilled nitric and hydrochloric acids or hydrofluoric acid and a double spike of ^{61}Ni and ^{62}Ni was prepared with a ^{61}Ni/^{62}Ni ratio of approximately 1. Both Ni isotope composition and concentrations were determined using a Neptune multi-collector inductively coupled plasma-mass spectrometer (MC-ICP-MS) with NIST standard SRM-986 used as a reference material. Depending on the concentration of Ni in the sample, 50 to 250 mg of sample powder was repeatedly digested in a mixture of HNO_3 and HCl or HF to dissolve sulfides and silicates, respectively, and evaporated to dryness to ensure complete digestion as described in Gueguen et al. (2013). The remaining residue was then dissolved in 10 mL of 6 mol/L HCl and one drop of H_2O_2 to ensure complete oxidation of Fe. Following the complete digestion of sulfide and silicate minerals and oxidation of Fe, Ni was purified using a two-stage process (Gueguen et al., 2013). First metals, including Fe, Zn, and most Co and Cu were trapped on an anionic resin (AG1-X8). The eluate, containing Ni and other matrix elements, was subsequentially evaporated and loaded onto a Ni-specific resin commercially available from Eichrom (Ni-Spec). The Ni was eluted quantitatively from the resin in HNO_3 and prepared for analysis.

Isotope analyses were performed using MC-ICP-MS allowing simultaneous measurement of ^{58}Ni, ^{60}Ni, ^{61}Ni, ^{62}Ni, and ^{57}Fe (to account for isobaric interference). Analysis was completed at

medium-resolution mode to resolve argide and oxide interferences on Ni and Fe isotopes. The main potential interferences are from ^{58}Fe on ^{58}Ni and ^{40}Ar^{18}O on ^{58}Ni. Correction for potential ^{58}Fe-interference was applied (Gueguen et al. 2013), but it was always less than 0.1‰. Ni isotope values with respect to SRM-986 are presented as:

$$\delta^{60}Ni = \left(\frac{^{60}Ni/^{58}Ni_{sample}}{^{60}Ni/^{58}Ni_{SRM-986}} - 1 \right) \times 1000 \quad and\ expressed\ in\ ‰ \qquad (1)$$

Typical instrumental precision achieved on Ni isotope ratios is better than 0.02 ‰ (calculated as two standard deviations of 26 replicate measurements of NIST SRM 986 during the same analytical session). Precision for delta measurements for each sample reported in Table 1 is calculated as two-standard deviation of replicate measurements of at least 5 delta values and ranged from less than 0.02 to 0.07 ‰. Ni isotope measurements of United States Geological Survey (USGS) Mn-nodule geostandards Nod-A-1 and Nod-P-1 were performed as unknown samples and we obtained δ^{60}Ni = 1.09 ± 0.06 ‰ and 0.41 ± 0.06 ‰, respectively, similar within uncertainty to previously published values (e.g. Gueguen et al. 2016). We also measured internal Ni standard solutions (Spex solution) after complete Ni separation through the columns and we obtained δ^{60}Ni =0.04 ± 0.04 ‰, identical within uncertainty to unprocessed standard solution. Procedural blanks were measured for each sample batch, and we obtained natural/spike ratio of less than 0.002, corresponding to less than 0.8 ng (compared to >400 ng of typical Ni samples), and therefore negligible.

4 Results

Major and trace element geochemical results for these samples were already presented in Hiebert et al. (2016), and some of the relevant data from that study is also included here (Table 1). New data is comprised of Ni concentrations and Ni isotopic values.

4.1 Ni concentrations and isotopic values

Barren komatiite samples contain between 774 and 2,690 ppm Ni, and have δ^{60}Ni values that range from -0.49 to +0.14‰. Samples with <10% sulfide minerals contain between 1,470 and 8,510 ppm Ni, and have δ^{60}Ni values that range from -0.57 to +0.11‰. Samples with 10-30% sulfide minerals contain between 7,910 and 35,100 ppm Ni, and have δ^{60}Ni values that range from -0.54 to -0.42‰. Samples with 30-70% sulfide minerals contain between 3,030 and 9,850 ppm Ni, and have δ^{60}Ni values that range from -1.06 to -0.27‰. Samples with >70% sulfide minerals contain between 8,380 and 39,300 ppm Ni, and have δ^{60}Ni values that range from -1.01 to -0.08‰ (Table 1; Fig. 6). These data are comparable in the range of values to those of other studies (Fig. 7; Saunders et al. 2020). The δ^{60}Ni values do not seem to be directly related to Ni concentration or Ni/S (Fig. 6b).

5 Discussion

Several mechanisms for fractionation of Ni isotopes have been suggested in the literature and might be applicable to komatiite-associated Fe-Ni-Cu-sulfide mineralization. High-temperature isotope fractionation between sulfide xenomelt and silicate melt does not explain the range of Ni isotope values of about 0.9‰ observed in komatiites at the Hart deposit and elsewhere (Agnew-Wiluna – Western Australia/Abitibi greenstone belt - Canada: Gueguen et al., 2013;

Zimbawe: Hofmann et al., 2014). Recent theoretical calculations of the reduced partition function ratios of $^{60}Ni/^{58}Ni$ have however revealed that the expectedrange of $\delta^{60}Ni$ values among Ni-bearing magmatic sulfides at 1156^{o}C is about 0.23‰ (Liu et al., 2018), near the temperature of initial monosulfide solid-solution (MSS) crystallization (Kitakaze et al. 2016; Mansur et al. 2021). In this study, we propose a two-step model that is capable of producing both the anomalously negative $\delta^{60}Ni$ values in komatiite-associated sulfides and the observed wide range of values for these sulfides through isotopic exchange between komatiitic magma and sulfide xenomelt during magma emplacement followed by fractional crystallization of the sulfide melt. This process was followed locally by carbonate alteration that could be responsible for sulfur-loss and samples with Ni/S greater than that of pentlandite, as these samples contain extremely low concentrations of sulfur. The samples with the highest Ni/S ratio, which could have undergone S-loss, have $\delta^{60}Ni$ values from -0.08 to +0.14‰, which is within the range of other komatiite samples with low-sulfide contents (Fig 6b). Additionally, other samples that have undergone carbonitization alteration, but have higher S concentrations, do not stand as outliers in the Ni, $\delta^{60}Ni$ or Ni/S data. Furthermore, a previous study noted that the Ni-Fe-S ratios remained in the igneous field and have not been significantly altered at Hart (Barnes and Naldrett 1987), suggesting that S mobility was limited, and Ni concentrations and isotopic ratios were not significantly affected by the carbonate alteration.

5.1 Stage 1: Isotopic fractionation and exchange between komatiitic lava and sulfide melt

During the eruption of komatiitic lavas at Hart, the lavas thermomechanically eroded their substrate producing a large channel that led to the formation of a sulfide xenomelt derived from sedimentary sulfides within the footwall rocks (Hiebert et al. 2016). This sulfide xenomelt

then scavenged Ni, Cu, and PGE from the komatiitic lava (Lesher and Campbell 1993; Lesher and Burnham 2001), leading to isotope exchange and fractionation of all relevant elements (e.g. S, Fe, Cu, and Ni; Fig. 8a; Ripley and Li 2003). To estimate the degree of Ni isotope fractionation between the komatiitic lava and sulfide xenomelt requires some knowledge of the magnitude of Ni-isotope fractionation between the silicate and sulfide liquids, however, many questions remain as to the magnitude and mechanism for this fractionation (e.g. Gueguen et al. 2013; Hofmann et al. 2014). Previous studies have shown that Ni isotope fractionation between silicates and Ni metal alloys can produce fractionation of +0.106‰ between silicate and metal at 1,200°C (Lazar et al. 2012). Here, we assume that a similar magnitude of equilibrium fractionation applies to silicate and sulfide liquids in komatiitic systems such that the sulfide melt would have δ^{60}Ni values 0.106‰ lower than the silicate melt once thermodynamic equilibrium is reached, which would produce a sulfide melt with δ^{60}Ni = -0.056‰ following isotope exchange with the mass of silicate melt being 50x the mass of sulfide melt as suggested by Hiebert et al. (2016) based on the modelling results (see Table 3 for model parameters). This also assumes that any fractionation between the silicate lava and crystallizing olivine is negligible. If crystallization of olivine corresponds to a significant fractionation, the δ^{60}Ni of the lava would likely be lower due to the preferential removal of heavier isotopes of Ni with the olivine crystals relative to the liquid melt resulting in an overall shift to more negative values in our model. Samples with high Ni/S ratios may have formed at higher silicate/sulfide mass ratios (up to 250x; Hiebert et al. 2016), which would shift the model to lower overall δ^{60}Ni values. We assumed that at the temperature of 1,200°C the komatiite lava is sufficiently crystallized to become isolated from the sulfide liquid, thus preventing subsequent isotopic exchange.

Further, in the case of net-textured sulfides, this temperature might be lower and the fractionation factor might be larger. In addition, the magnitude of fractionation between silicate and sulfide melts might not be the same as that between metal and silicate. However, our calculations are only meant to demonstrate the plausibility of the inferred mechanism for fractionation and are not based on exact (currently poorly constrained) values of fractionation factors.

5.2 Stage 2: Fractional crystallization of sulfide melt

Due to the lower crystallization temperature of sulfides than that of olivine-rich komatiite, with olivine crystallization giving way to pyroxene crystallization at ~1180°C and crystallization of MSS beginning at ~1150°C (Fleet 2006; Arndt et al. 2008), the sulfide melt would begin to crystallize after the silicate melt had partially to completely solidified, probably sufficiently to create a barrier of olivine crystals between the residual silicate and sulfide liquids, limiting further isotopic exchange (Fig. 8b). Although there may be minor exchange with trapped interstitial silicate liquids in the olivine cumulate rocks, the pyroxenitic komatiite at Hart does not contain sulfide minerals, suggesting that if sulfides were in contact with silicate melt below ~1180°C, it was in a very small volume. As a result, isotopic equilibrium with silicate melt would not be maintained during cooling and crystallization of sulfide melt. During crystallization of sulfide, shorter Ni-Ni and Ni-S bonds in the sulfide crystals, relative to the liquid, induce fractionation of the heavier isotopes of Ni into the crystal phase, and, based on theoretical considerations, a δ^{60}Ni fractionation of 0.23‰ between sulfide crystals and a gas phase could occur at 1156^{o}C (Liu et al. 2018), the temperature of crystallization of MSS from sulfide liquid (Kitakaze et al. 2016; Mansur et al. 2021). The calculations based on sulfide crystals exchanging

with a gas phase may not be directly analogous to crystallization from a liquid and the magnitude of fractionation is likely to be smaller between a liquid and sulfide crystals compared with that between a gas and sulfide crystals. However, the magnitude of this difference is not known. Additionally, the addition of Fe to the sulfide system was shown to increase the amount of fractionation between sulfide crystals and gas in theoretical calculations (Liu et al. 2018). However, the calculations did not extrapolate to high enough Fe:Ni ratios to mimic sulfide mineralization relevant to that hosted by komatiites, and so the actual magnitude of this effect is also unknown. As such, we are simply attempting to demonstrate the plausibility of the mechanism, without the exactly known fractionation factors involved, and we assume that the effects of the difference between gas and liquid and higher concentrations of Fe in a natural system will at least partially offset each other. We thus used a fractionation factor of $\Delta_{melt\text{-}min}$ = -0.23‰ at 1156°C (Liu et al. 2018) that that enriches the residual sulfide melt in the lighter Ni isotopes during crystallization of the sulfide liquid.

Mungall (2007) modelled the crystallization of sulfide liquids at the Sudbury Igneous Complex, and found that the sulfide mineralization is not a product of a quenched liquid, but instead represents sulfide mineral cumulates, with the most fractionated material removed. Based on a cumulate model (e.g., McBirney and Noyes 1979), the crystallization of sulfide liquids would begin at a stagnant boundary layer in contact with the colder footwall rocks at the base of the sulfide liquid and the crystallization front would migrate upwards as cooling progressed (Fig. 8c). This would allow the denser sulfide crystals, with some trapped liquid, to accumulate and become isolated from the remaining sulfide melt by a stagnant boundary layer promoting Rayleigh fractionation of Ni isotopes between the melt and crystals as crystallization

progressed. As the melt is enriched in lighter isotopes of Ni relative to the sulfide crystals formed, increasing amount of trapped liquid will progressively create more negative δ^{60}Ni values in sulfides. In our modelling with up to 30% of trapped liquid, this process could create a range of δ^{60}Ni values from +0.15‰ at 1% crystallized with no trapped liquid to -1.02‰ at 99% crystallized with 30% of trapped liquid that encompasses nearly all the data for samples that are described as having >30% sulfide minerals (referred to as high-sulfide samples) in this and other studies (-1.06 to -0.08‰; Fig. 9; Tanimizu and Hirata 2006, Gueguen et al. 2013; Hofmann et al. 2014; see Table 3 for model parameters). A model for equilibrium (batch) crystallization of the sulfide melt, in which crystals separate from the melt after varying degrees of crystallization, can only produce significant negative values with very low degrees of crystallization, but cannot produce the entire range of values from the previously mentioned data (Fig. 9).

The only sample of sulfide that does not fall within the range corresponding to any degree of fractionation in this model is a sample of millerite from Thompson, Manitoba, Canada (Tanimizu and Hirata 2006), with a value of +0.7‰. The Thompson deposit is well known to be strongly structurally and hydrothermally modified and metamorphosed to a significantly higher grade than the other deposits so far studied (e.g. Layton-Matthews et al. 2010). As such, this sample may have been subject to additional fractionation processes during hydrothermal alteration, remobilization, and metamorphism, although the effects of these processes are not well understood and constrained. Thus far, mantle metasomatism of samples lacking sulfide has been examined, a significantly different process from the hydrothermal alteration observed at the Thompson deposit, showing only marginal fractionation (Klaver et al. 2020). However, the

study did note that the metasomatized samples appear to be in disequilibrium, hence the δ^{60}Ni values of the Thompson sample may have been affected by some process during regional metamorphic metasomatism, such as the introduction of Ni with a different isotopic composition by the fluid, changes in mineralogy of the Ni-sulfides, or disequilibrium.

The proposed model for the fractionation of Ni isotopes to produce the wide range of δ^{60}Ni values predicts that earlier crystallized sulfides will have higher δ^{60}Ni values, whereas later crystallizing sulfides will have lower Ni isotope values. Past studies have shown that pentlandite forms over a range of temperatures, through peritectic reactions and subsolidus exsolution (Kelly and Vaughan 1983; Kitakaze et al. 2016; Mansur et al. 2019), and further fractionation between pentlandite and MSS or the evolving sulfide liquid could occur during these processes. This could be further tested with *in situ* measurements of δ^{60}Ni values of sulfide minerals in significant accumulations of sulfides to model the crystallization path of sulfides, which should crystallize sulfides with progressively more lighter Ni isotope values along the crystallization path from early to late crystallizing mineral phases (Ebel and Naldrett 1997; Fleet 2006), and could resolve whether fractionation of Ni isotopes occurs during the peritectic reactions and/or exsolution of pentlandite during cooling. A stepwise shift from this pattern would indicate an interruption in the crystallization process related to rapid flushing out of liquid and resupply of new magma batch. With our data we are able to make a preliminary assessment of this based on profiles from three drill cores (Fig. 10), although significantly higher sampling resolution is needed to thoroughly investigate this. In a simple profile of decreasing sulfide proportion upward from the base of the komatiite, as in drill-core H08-96 (Fig. 10a), the expected pattern of increasing δ^{60}Ni values is observed. However, in profiles with a more complex pattern of

changes in the proportion of sulfide, as in drill-holes H11-05 and H08-80, the pattern of δ^{60}Ni values is also more complex and could indicate interruptions in the crystallization process (Figs. 10b and 10c).

The model could also have an exploration relevance, with higher than BSE δ^{60}Ni values in komatiite indicating that it has equilibrated with significant sulfide mineralization upstream. Furthermore, sulfides with anomalously low (<-2.0‰) or high (>+0.0‰) δ^{60}Ni values in small sulfide accumulations could be an indication of post-mineralization alteration of the sulfide body, as is inferred for the millerite sample from Thompson in Manitoba, Canada (Tanimizu and Hirata 2006).

6 Conclusions

A large range of predominantly negative δ^{60}Ni values is observed in the Hart komatiite-associated sulfide mineralization in the Abitibi greenstone belt. The observed large range with negative values of δ^{60}Ni in komatiite associated sulfide mineralization can be attributed to a two-stage process of fractionation during isotopic exchange between komatiitic lava and sulfide melt followed by fractional crystallization of cumulus sulfide minerals from the sulfide melt. Such a model produces variability of δ^{60}Ni values from -1.02 to +0.15‰, consistent with the observed range of values for non-remobilized and undeformed sulfides of low metamorphic grade from this and other studies of -1.06 to -0.08‰.

7 Acknowledgements

We express our appreciation to Northern Sun Mining Corp. (formerly Liberty Mines Ltd.) for their logistical support, access to properties, information, and discussions with staff throughout this project. Financial support for this project has been provided by the Targeted Geoscience Initiative-4 program of the Geological Survey of Canada and Natural Sciences and Engineering Research Council of Canada (NSERC) Discovery and Accelerator Grants to AB. This manuscript benefitted from the careful and insightful reviews of Dr. James Scoates, an anonymous reviewer, and Dr. Michael Lesher, and editorial handling of Dr. Catherine Chauvel.

Declaration of interests

The authors declare that they have no known competing financial interests or personal relationships that could have appeared to influence the work reported in this paper.

8 References

Archer, C., Vance, D., Milne, A., Lohan, M. C. 2020. The oceanic biogeochemistry of nickel and its isotopes: New data from the South Atlantic and the Southern Ocean biogeochemical divide. Earth and Planetary Science Letters 535 116118.

Arndt, N.T., Lesher, C.M., Barnes, SJ. 2008. Komatiite. Cambridge University Press, New York, 467 pp.

Barnes, S-J., Naldrett, A.J. 1987. Fractionation of the platinum-group elements and gold in some komatiites of the Abitibi greenstone belt, Northern Ontario. Economic Geology 82, 165-183.

Cameron, V., Vance, D. 2014. Heavy nickel isotope compositions in rivers and the oceans. Geochimica et Cosmochimica Acta 128, 195-211.

Cameron, V., Vance, D., Archer, C., House, C.H. 2009. A biomarker based on the stable isotopes of nickel. Proceedings of the National Academy of Sciences of the United States of America 106, 10944-10948.

Campbell, I.H., Naldrett, A.J. 1979. The influence of silicate:sulfide ratios on the geochemistry of magmatic sulfides. Economic Geology 75, 1503-1506.

Chen, H., Savage, P.S., Teng, F.Z., Helz, R.T., Moynier, F. 2013. Zinc isotope fractionation during magmatic differentiation and the isotopic composition of the bulk Earth. Earth and Planetary Science Letters 369, 34-42.

Christoffersen, P. 2017. Stable Cu, Fe, and Ni isotopic systematics of the Sudbury offset dikes and associated rocks. Unpublished M.Sc. thesis, University of Western Ontario, 100pp.

Ciscato, E. R., Bontognali, T. R. R., Vance, D. 2018. Nickel and its isotopes in organic-rich sediments: implications for oceanic budgets and a potential record of ancient seawater. Earth and Planetary Science Letters 494, 239–250.

Duke, J.M. 1979. Computer simulation of the fractionation of olivine and sulfide from mafic and ultramafic magmas. Canadian Mineralogist 76, 507-514.

Duke, J.M., Naldrett, A.J. 1978. A numerical model of the fractionation of olivine and molten sulfide from komatiite magma. Earth and Planetary Science Letters 39, 255-266.

Ebel, D.S., Naldrett, A.J. 1997. Crystallization of sulfide liquids and the interpretation of ore composition. Canadian Journal of Earth Sciences 34, 352-365.

Elliott, T., Steele, R.C.J. 2017. The isotope geochemistry of Ni. In: F-Z. Teng, J. Watkins, N. Dauphas (eds.). Reviews in Mineralogy & Geochemistry 82, 511-542.

Estrade, N., Cloquet, C., Echevarria, G., Sterckeman, T., Deng, T., Tang, YeTa, Morel, J.-L. 2015. Weathering and vegetation controls on nickel isotope fractionation in surface ultramafic environments (Albania). Earth and Planetary Science Letters 423, 24–35.

Faure, G. 1998. Principles and applications of geochemistry, 2nd Ed. Prentice Hall, 600pp.

Fleet, M.E. 2006. Phase equilibria at high temperatures. In: D.J. Vaughan (ed) Reviews in Mineralogy and Geochemistry 61, 365-419.

Gall, L. 2011. Development and application of nickel stable isotopes as a new geochemical tracer. Ph.D. thesis, University of Oxford. 245p.

Gall, L., Williams, H. M., Siebert, C., Halliday, A. N., Herrington, R. J., Hein, J. R. 2013. Nickel isotopic compositions of ferromanganese crusts and the constancy of deep ocean inputs and continental weathering effects over the Cenozoic. Earth and Planetary Science Letters 375, 148–155.

Gall, L., Williams H. M., Halliday A. N., Kerr A. C. 2017. Nickel isotopic composition of the mantle. Geochimica et Cosmochimica Acta 199, 196–209.

Gueguen, B., Rouxel, O., Ponzevera, E., Bekker, A., Fouquet, Y. 2013. Nickel isotope variations in terrestrial silicate rocks and geological reference materials measured by MC-ICP-MS. Geostandards Geoanalytical Research 37, 297–317.

Gueguen, B., Rouxel, O., Rouget, M.-L., Bollinger, C., Ponzevera, E., Germain, Y., Fouquet, Y. 2016. Comparative geochemistry of four ferromanganese crusts from the Pacific Ocean and significance for the use of Ni isotopes as paleoceanographic tracers. Geochimica et Cosmochimica Acta 189, 214–235.

Geuguen, B., Sorensen, J.V., Lalonde, S.V., Pena, J., Toner, B.M., Rouxel, O. 2018. Variable Ni isotope fractionation between Fe-oxyhydroxides and implications for the use of Ni isotopes as geochemical tracers. Chemical Geology 481, 38-52.

Hiebert, R.S., Bekker, A., Wing, B.A., Rouxel, O.J. 2013. The role of paragneiss assimilation in the origin of the Voisey's Bay Ni-Cu sulfide deposit, Labrador: multiple S and Fe isotope evidence. Economic Geology 108, 1459-1469.

Hiebert, R.S., Bekker, A., Houlé, M.G., Wing, B.A., Rouxel, O.J. 2016. Tracing sources of crustal contamination using multiple S and Fe isotopes in the Hart komatiite-associated Ni-Cu-(PGE) sulphide deposit, Abitibi greenstone belt, Ontario, Canada. Mineralium Deposita 51, 919-935.

Hiebert, R.S., Bekker, A. Houlé, M.G., Rouxel, O.J. 2018. Depositional setting of the Late Archean Fe oxide- and sulfide-bearing chert and graphitic argillite in the Shaw Dome, Abitibi greenstone belt, Canada. Precambrian Research 311, 98-116.

Hofmann, A., Bekker, A., Dirks, P., Gueguen, B., Rumble, D., Rouxel, O.J. 2014. Comparing orthomagmatic and hydrothermal mineralization models for komatiite-hosted nickel deposits in Zimbabwe using multiple-sulfur, iron, and nickel isotope data. Mineralium Deposita 49, 75-100.

Houlé, M.G., Lesher, C.M. 2011. Komatiite-associated Ni-Cu-(PGE) deposits, Abitibi greenstone belt, Superior Province, Canada. In: C. Li, E.M. Ripley (eds.). Magmatic Ni-Cu and PGE deposits: geology, geochemistry, and genesis, Society of Economic Geologists, Reviews in Economic Geology 17, 89-121.

Houlé, M.G., Gibson, H.L., Lesher, C.M., Davis, P.C., Cas, R.A.F., Beresford, S.W., Arndt, N.T. 2008. Komatiitic sills and multigenerational peperite at Dundonald Beach, Abitibi greenstone belt, Ontario: volcanic architecture and nickel sulfide distribution. Economic Geology 103, 1269-1284.

Houlé, M.G., Préfontaine, S., Fowler, A.D., Gibson, H.L. 2009. Endogenous growth in channelized komatiite lava flows: evidence from spinifex-textured sills at Pyke Hill and Serpentine Mountain, western Abitibi greenstone belt, northeastern Ontario, Canada. Bulletin of Volcanology 71, 881-901.

Houlé, M.G., Lesher, C.M., Gibson, H.L., Ayer, J.A. and Hall, L.A.F. 2010a. Localization of komatiite-associated Ni-Cu-(PGE) deposits in the Shaw Dome, Abitibi greenstone belt, Superior Province; in Abstracts, 11th International Platinum Symposium, 21–24 June 2010, Sudbury, Ontario, Canada, Ontario Geological Survey, Miscellaneous Release—Data 269.

Houlé, M.G., Lesher, C.M., Préfontaine, S., Ayer, J.A., Berger, B.R., Taranovic, V., Davis, P.C. and Atkinson, B. 2010b. Stratigraphy and physical volcanology of komatiites and associated Ni-Cu-(PGE) mineralization in the western Abitibi greenstone belt, Timmins area, Ontario: a field trip for the 11th International Platinum Symposium; Ontario Geological Survey, Open File Report 6255, 99p.

Houlé, M.G., Lesher, C.M., Davis, P.C. 2012. Thermomechanical erosion at the Alexo Mine, Abitibi greenstone belt, Ontario: implications for the genesis of komatiite-associated Ni-Cu-(PGE) mineralization. Mineralium Deposita 47, 105-123.

Huppert, H.E., Sparks, R.S.J., Turner, J.S., Arndt, N.T. 1984. Emplacement and cooling of komatiite lavas, Nature 309, 19-22.

Jolly, W.T. 1982. Progressive metamorphism of komatiites and related Archaean lavas of the Abitibi area, Canada. In: N.T. Arndt, E.G. Nisbet (eds) Komatiites. p. 247-266.

Kelly, D.P., Vaughan, D.J. 1983. Pyrrhotine-pentlandite ore textures: a mechanistic approach. Mineralogical Magazine 47, 453-463.

Kitakaze, A., Machida, T., Komatsu, R. 2010. Phase relations in the Ni-Fe-S system from 875 to 650°C. Canadian Mineralogist 54, 1175–1186.

Klaver, M., Ionov, D.A., Takazawa, E., Elliott, T., 2020. The non-chondritic Ni isotope composition of Earth's mantle. Geochimica et Cosmochimica Acta 268, 405-421.

Layton-Matthews, D., Lesher, C.M., Burnham, O.M., Hulbert, L., Peck, D.C., Golightly, J.P., Keays, R.R. 2010. Exploration for komatiite-associated Ni-Cu-(PGE) mineralization in the Thompson Nickel Belt, Manitoba. In: R.J. Goldfarb, E.E. Marsh T. Monecke (eds) Society of Economic Geology Special Publication Number 15, Volume II, p. 513-538.

Lazar, C., Young, E.D., Manning, C.E. 2012. Experimental determination of equilibrium nickel isotope fractionation between metal and silicate from 500 ^{o}C to 950 ^{o}C. Geochimica et Cosmochimica Acta 86, 276-295.

Lesher, C.M. 1989. Komatiite-associated nickel sulfide deposits. In: J.A. Whitney and A.J. Naldrett (eds.) Ore Deposition Associated with Magmas. Pp. 45-102. Dordrecht: Society of Economic Geologists.

Lesher, C.M. 2017. Roles of xenomelts, xenocrysts, xenovolatiles, residues, and skarns in the genesis, transport, and localization of magmatic Fe-Ni-Cu-PGE sulfides and chromite. Ore Geology Reviews 90, 465-484.

Lesher, C.M., Campbell, I.H. 1993. Geochemical and fluid dynamic modeling of compositional variations in Archean komatiite-hosted nickel sulfide ores in Western Australia; Economic Geology 88, 804-816.

Lesher, C.M., Groves, D.I. 1986. Controls on the formation of komatiite-associated nickel-copper sulfide deposits. In: G.H. Friedrich (ed.) Geology and Metallogeny of Copper Deposits. Springer-Verlag, Berlin.

Lesher, C.M., Stone, W.E. 1996. Exploration geochemistry of komatiites. *In:* Wyman, D.A. ed., Igneous Trace Element Geochemistry Applications for Massive Sulphide Exploration: Geological Association of Canada, Short Course Notes, v. 12, 153-204.

Lesher, C.M., Burnham, O.M. 2001. Multicomponent elemental and isotopic mixing in Ni-Cu-(PGE) ores at Kambalda, Western Australia; The Canadian Mineralogist 39, 421-446.

Lesher, C.M., Arndt, N.T., Groves, D.I., 1984. Genesis of komatiite-associated nickel sulphide deposits at Kambalda, Western Australia: a distal volcanic model, in: Buchanan, D.L., Jones, M.J. (Eds.), Sulphide Deposits in Mafic and Ultramafic Rocks. Inst. Min. Metall., London, 70–80.

Liu, S., Li, Y., Ju, Y., Liu, J., Liu, J., Shi, Y. 2018. Equilibrium nickel isotope fractionation in nickel sulfide minerals. Geochimica et Cosmochimica Acta 222, 1-16.

Mansur, E.T., Barnes, S.-J. And Duran, C.J. 2019. Textural and compositional evidence for the formation of pentlandite via peritectic reaction: Implications for the distribution of highly siderophile elements. Geology 47, 351-354.

Mansur, E.T., Barnes, S.-J., Duran, C.J. 2021. An overview of chalcophile element contents of pyrrhotite, pentlandite, chalcopyrite, and pyrite from magmatic Ni-Cu-PGE sulfide deposits. Mineralium Deposita 56, 179-204.

McBirney, A.R., Noyes, R.M. 1979. Crystallization and layering of the Skaergaard Intrusion. Journal of Petrology 20, 487-554.

Pašava J., Chrastny´ V., Loukola-Ruskeeniemi K., Šebek O. 2019. Nickel isotopic variation in black shales from Bohemia, China, Canada, and Finland: a reconnaissance study. Mineralium Deposita 54, 719–742

Porter, S. J., Selby, D., Cameron, V. 2014. Characterising the nickel isotopic composition of organic-rich marine sediments. Chemical Geology 387, 12–21.

Pyke, D.R., Naldrett, A.J., Eckstrand, O.R. 1973. Archean ultramafic flows in Munro Township, Ontario. Geological Society of America Bulletin 84, 955-978.

Ratié, G., Jouvin, D., Garnier, J., Rouxel, O., Miska, S., Guimarães, E., Cruz Vieira, L., Sivry, Y., Zelano, I., Montarges-Pelletier, E., Thil, F., Quantin, C. 2015. Nickel isotope fractionation during tropical weathering of ultramafic rocks. Chemical Geology 402, 68-76.

Ratié, G., Quantin, C., Jouvin, D., Calmels, D., Ettler, V., Sivry, Y., Vieira, L. C., Ponzevera, E., Garnier, J. 2016. Nickel isotope fractionation during laterite Ni ore smelting and refining: Implications for tracing the sources of Ni in smelter-affected soils. Applied Geochemistry 64, 136–145.

Ratié, G., Quantin, C., Maia De Freitas, A., Echevarria, G., Ponzevera, E., Garnier, J. 2019. The behavior of nickel isotopes at the biogeochemical interface between ultramafic soils and Ni accumulator species. Journal of Geochemical Exploration 196, 182–191.

Ripley, E.M., Li, C. 2003. Sulfur isotope exchange and metal enrichment in the formation of magmatic Cu-Ni-(PGE) deposits. Economic Geology 98, 635-641.

Ripley, E.M., Li, C. 2013. Sulfide saturation in mafic magmas: is external sulfur required for magmatic Ni-Cu-(PGE) ore genesis? Economic Geology 108, 45-58.

Saunders, N.J., Barling, J., Harvey, J., Halliday, A.N. 2020. Heterogeneous nickel isotopic compositions in the terrestrial mantle – Part 1: Ultramafic lithologies. Geochimica et Cosmochimica Acta 285, 129-149.

Savage, P., Moynier, F., Chen, H., Shofner, G., Siebert, J., Badro, J., Puchtel, I.S. 2015. Copper isotope evidence for large-scale sulphide fractionation during Earth's differentiation. Geochemical Perspectives Letters 1, 53–64.

Sergeev, S., Kapitonov, I., Krymsky, R., Adamskaya, E., Goltsin, N. 2019. Copper and nickel isotopes. In: Petrov, O. (ed) Isotope Geology of the Norilsk Deposits. Springer Geology, 73-88.

Spivak-Birndorf, L. J., Wang, S.-J., Bish, D. L., Wasylenki L. E. 2018. Nickel isotope fractionation during continental weathering. Chemical Geology 476, 316–326.

Steele R. C. J., Elliott T., Coath C. D., Regelous M. 2011. Confirmation of mass-independent Ni isotopic variability in iron meteorites. Geochimica et Cosmochimica Acta 75, 7906–7925.

Tanimizu, M., Hirata, T. 2006. Determination of natural isotopic variation in nickel using inductively coupled plasema mass spectrometry. Journal of Analytical Atomic Spectrometry 21, 1423-1426.

Thompson, P.H. 2005. A new metamorphic framework for gold exploration in the Timmins–Kirkland Lake area, western Abitibi greenstone belt: Discover Abitibi Initiative. Ontario Geological Survey, Open File Report 6162, 104 p.

Thurston, P.C., Ayer, J.A., Goutier, J. 2008. Depositional gaps in Abitibi greenstone belt stratigraphy: a key to exploration for syngenetic mineralization. Economic Geology 103, 1097–1134.

Urey, H.C. 1947. The thermodynamic properties of isotopic substances. Journal of the Chemical Society 1947, 562–581.

Vance, D., Little, S. H., Archer, C., Cameron, V., Andersen, M. B., Rijkenberg, M. J. A., Lyons T. W. 2016. The oceanic budgets of nickel and zinc isotopes: the importance of sulfidic environments as illustrated by the Black Sea. Philosophical Transactions of the Royal Society A, 374.

Ventura, G. T., Gall, L., Siebert, C., Prytulak, J., Szatmari, P., Hürlimann M., Halliday, A. N. 2015. The stable isotope composition of vanadium, nickel, and molybdenum in crude oils. Applied Geochemistry 59, 104–117.

Wang, R.-M., Archer, C., Bowie, A. R., Vance D. 2019. Zinc and nickel isotopes in seawater from the Indian Sector of the Southern Ocean: the impact of natural iron fertilization versus Southern Ocean hydrography and biogeochemistry. Chemical Geology 511, 452–464

Figure and table captions

Figure 1: Simplified geological map showing the main komatiite-associated Ni-Cu-(PGE) mineralization, including the Hart deposit, within the Shaw Dome area in the Abitibi greenstone belt (modified from Houlé et al. 2010a, b).

Figure 2: Simplified geologic map of the Hart deposit area (modified from Houlé et al. 2010b). Approximate collar locations of sampled drill holes. Coordinates in UTM NAD83 Zone 17.

Figure 3: Cross-section diagrams along local grid (a) 2400E, (b) 2425/2450E and (c) 2900E showing the simplified geology of each diamond drill core examined in this study and sample positions (indicated by sample number and black star).

Figure 4: Reflected light photomicrographs showing the textures of sulfides from the Hart deposit: (a) disseminated sulfide (H11-13C-282.8), (b) net-textured, semi-massive sulfide (H11-05-57.1); (c) semi-massive and massive sulfide (H11-05-62.6). Po – pyrrhotite, Mt – magnetite, Sil – silicate minerals, Cb – carbonate minerals.

Figure 5: Photomicrographs showing the mineralogy and textures of samples from the Hart deposit. (a) typical relict olivine cumulate texture in sample H11-08-10.45 (not analyzed in this study), and (b) poorly preserved olivine cumulate texture due to carbonatization alteration (H11-13C-282.8). Sample H11-05-61.1 shows relict olivine cumulate textures and is typical of samples from the Hart deposit (PPL in c, XPL in d). Sample H11-05-62.6 contains higher than normal and larger tremolite crystals (PPL in e, XPL in f). Carbonate alteration in sample H11-13C-265.85 with rhombohedrally shaped carbonate crystals (PPL in g, XPL in h). Act – actinolite; Atg – antigorite, Cb – carbonate, Ol – metamorphic olivine, Ol – opaque phases, Tr – tremolite.

Figure 6: Plots of (a) δ^{60}Ni vs. 1/Ni, (b) δ^{60}Ni vs. Ni/S, and (c) Ni vs. S. Also plotted in (b) and (c) is the stoichiometric relationship between Ni and S for the observed sulfide minerals, pyrrhotite (po) and pentlandite (pn). Weakly serpentine±carbonatized (serp±cbz) altered samples are indicated by quarter-black symbols, and stronger serpentine-carbonatization (serp-cbz) alteration by half-black symbols.

Figure 7: Compilation of published δ^{60}Ni data for terrestrial samples and estimates of bulk silicate earth (BSE) modified from Saunders et al. (2020) with the data from this study added. Symbols for the data from this study are as in Fig. 4. [1]Tanimizu and Hirata (2006); [2]Cameron et al. (2009); [3]Gall (2011); [4]Steele et al. (2011); [5]Gueguen et al. (2013); [6]Gall et al. (2013); [7]Cameron and Vance (2014); [8]Porter et al. (2014); [9]Hofmann et al. (2014); [10]Ratié et al. (2015); [11]Estrade et al. (2015); [12]Ventura et al. (2015); [13]Ratié et al. (2016); [14]Vance et al. (2016); [15]Gueguen et al. (2016); [16]Gall et al. (2017); [17]Elliott and Steele (2017); [18]Spivak-Birndorf et al. (2018); [19]Ciscato et al. (2018); [20]Ratié et al. (2019); [21]Wang et al. (2019); [22]Pašava et al. (2019); [23]Klaver et al. (2020); [24]Archer et al. (2020); [25]Christoffersen (2017).

Figure 8: Schematic model for the fractionation of Ni isotopes during (a) formation of sulfide xenomelt and isotopic exchange with komatiitic magma, (b) cooling of sulfide liquid after komatiite is partially to fully crystalline, and (c) fractional crystallization of sulfide liquid.

Figure 9: Model for producing a large range of δ^{60}Ni values in sulfides at the Hart deposit with melt (green) and sulfide solid isotopic composition controlled by fractional crystallization of sulfide melt with varying proportions of trapped liquid. Also shown is a model for equilibrium (batch) crystallization of the sulfide melt, in which crystals separate from the melt after varying degrees of crystallization.

Figure 10: Profiles of δ^{60}Ni across sulfide zones in individual drill cores from the Hart deposit.

Table 1: Summary of mineralogy and alteration for samples with geochemical and isotopic data for the Hart deposit.

Lithology	Sample	δ^{60}Ni (‰)	2 σ[1]	Ni (ppm)	S (wt %)[2]	Sulfide Abundance Classification	Sulfide Mineralogy	Silicate Textures	Metamorphism and Alteration[3]	Carbonatization	Non-sulfide Mineralogy[4]
Barren komatiite	H11-13C-339.	0.14	0.01	1030	0.0	Trace to no visble sulfides	±Po	Ol cumulate, well-preser	Serp ±Cbz	Minor to trace Cb stringers (<1-3%)	Atg, Tr, Chl, Chr

	1							ved			
	H07-33-251.2	-0.08	0.06	2690	0.2						
	H11-11-407	0.12	0.02	774	0.0			Ol cumulate, poorly-preserved	Serp-Cbz	Cb veinlets, Cb rhomboh edral crystals (15-25%)	Cb, Atg, Chl, Chr
	H11-13C-301.6[5]	0.14	0.06	897	0.1						
	H08-80-97.3	-0.49	0.07	2240	0.6						
	H11-13C-265.85	0.13	0.02	1860	0.5						
	H11-13C-301.6[5]	0.14	0.06	897	0.1			Oblite rated cumul ate	Amp	-	Tr, Chl, Chr
Komatiite with disseminated sulfides	H07-33-128.3	0.11	0.04	1490	1.1	<10% sulfides	Po-Pn	Ol cumulate, well-preserved	Serp	-	Atg, Tr, Chl, Chr, rare relict Cpx
	H08-96-259.6	-0.10	0.07	6080	1.2						
	H11-11-337.7	-0.21	0.05	6080	1.3						
	H11-13C-282.	-0.57	0.04	8510	1.3			Ol cumulate, poorly-	Serp-Cbz	Cb veinlets, Cb rhomboh edral	Cb, Atg, Chl, Chr

	8							preserved		crystals (15-25%)	
	H11-05-62.35	-0.49	0.04	1470	1.9			Obliterated cumulate	Amp	-	Tr, Chl, Chr
Komatiite with disseminated to blebby sulfides	H08-96-274.4	-0.54	0.05	7910	6.8	10-30% sulfides	Po-Pn	Ol cumulate, well-preserved	Serp	-	Atg, Tr, Chl, Chr, rare relict Cpx
	H11-11-352.6	-0.42	0.05	35100	8.9			Ol cumulate, poorly-preserved	Serp-Cbz	Cb veinlets, Cb rhomboh edral crystals (15-25%)	Cb, Atg, Chl, Chr
	H11-11-356.55	-0.48	0.04	16600	8.4						
Semi-massive sulfide (locally net-textured)	H11-05-57.1	-1.06	0.06	9560	15.0	30-70% sulfides	Po-Pn	Ol cumulate, well-preserved	Serp	-	Atg, Tr, Chl, Chr
	H08-80-134.65	-0.43	0.04	7410	15.9						
	H11-05-61.1	-0.32	0.06	3030	22.3						
Semi-massive sulfide (locally net-textured)	H11-05-62.6	-0.27	0.06	9850	22.0		Po-Pn	Obliterated cumulate	Amp	-	Tr, Chl, Chr, trace metamorphic Ol
Massive sulfide	H08-80-136	-0.46	0.03	13600	32.3	>70% sulfides	Po-Pn±Cp	-	-	-	Chr, Mt, Atg, Chl
	H08-80-114.25	-0.08	0.06	8380	35.0						

	H08-96-277.8[6]	-0.71	0.03	39300	41.0		Po-Pn-Py±Cp				
	H08-96-283.8[6]	-1.01	0.03	15300	49.3						
USGS standard	Nod-A-1	1.09	0.06	-	-	-	-	-	-	-	-
USGS standard	Nod-P-1	0.41	0.06	-	-	-	-	-	-	-	-

[1]Two standard deviation of replicate measurements of at least 5 delta values
[2]From Hiebert et al. (2016)
[3]Amp - amphibolitization; Cbz - carbonitization; Serp - serpentinization
[4]Atg - antigorite; Cb - carbonate; Chl - chlorite; Chr - chromite; Cpx - clinopyroxene; Mt - magnetite; Ol - olivine; Tr - tremolite
[5]H11-13C-301.6 listed twice due to the presence of both carb alteration and an+ increase in abundance of amphiboles and the absence of Atg in samples
[6]Samples H08-96-277.8 and H08-96-283.8 contain 15-20% pyrite as well as pyrrhotite and pentlandite

Table 2: Table of local grid and UTM coordinate of sampled drill hole collars.

DDH	Local Grid			UTM NAD83 Zone 17			Dip
	East	North	Azimuth	East	North	Azimuth	
H07-33	2425.6	3881	000	493998	5349954	330	-45
H08-80	2450	4000	000	493959.6	5350069	330	-47
H08-96	2400	3917.7	000	493957.5	5349973	330	-45
H11-05	2400	4075	000	493878.8	5350109	330	-57
H11-11	2900	3846	000	494426.3	5350161	330	-77
H11-13C	2900	3882	000	494405.3	5350197	330	-74

[1]Two standard deviation of replicate measurements of at least 5 delta values
[2]From Hiebert et al. (2016)
[3]Amp - amphibolitization; Cbz - carbonitization; Serp - serpentinization
[4]Atg - antigorite; Cb - carbonate; Chl - chlorite; Chr - chromite; Cpx - clinopyroxene; Mt - magnetite; Ol - olivine; Tr - tremolite
[5]H11-13C-301.6 listed twice due to the presence of both carb alteration and an+ increase in abundance of amphiboles and the absence of Atg in samples
[6]Samples H08-96-277.8 and H08-96-283.8 contain 15-20% pyrite as well as pyrrhotite and pentlandite

Table 3: Equations and values used to model the variability of δ^{60}Ni values in sulfides.

Stage 1: Equilibrium Ni fractionation between komatiite lava and sulfide xenomelt

Partitioning of Ni into sulfide[1]: $C_{sul} = \frac{C_{sul}^0 + C_{sil}^0 RD^{sul/sil}}{R + D^{sul/sil}}$				
C_{sil}^0=1077 ppm[2]	C_{sul}^0=200 ppm[2]	D=100 [1]	R=50 [2]	C_{sul}=36600 ppm[3]

Isotope Exchange[4]: $\delta^{60}Ni_{sul} = \frac{R^*(\delta^{60}Ni_{sil}^0 + \Delta)}{1+R^*}$ $R^* = \frac{C_{sil}^0}{C_{sul}^0} R$			
$\delta^{60}Ni_{sil}^0$=+0.05‰[3]	R*=270[2]	Δ=-0.106‰[3]	$\delta^{60}Ni_{sul}$=-0.056‰

Stage 2a: Fractional crystallization

$$\delta^{60}Ni_{melt} = \left(\delta^{60}Ni_{melt}^0 + 1000\right) f^{\alpha-1} - 1000 \quad (5)$$

$$\delta^{60}Ni_{crystals} = \alpha\left(\delta^{60}Ni_{melt}^0 + 1000\right) f^{\alpha-1} - 1000 \quad (5)$$

$\delta^{60}Ni_{melt}^0 = \delta^{60}Ni_{sul}$=-0.056‰	f= fraction of melt remaining	α=1.0023 ($\Delta_{melt\text{-}crystal}$=-0.23‰)[6]

Stage 2b: Effect of trapped liquid (using isotope exchange formula above)

R* is dependant of volume of trapped liquid (0.11 for 10%, 0.25 for 20% and 0.43 for 30%)

Stage 2c: Equilibrium, batch crystallization (using isotope exchange formula above) $R = \frac{f}{1-f}$

[1] *Equation and some of the parameters are from Lesher and Burnham 2001*
[2] *Initial concentrations of Ni in silicate and sulfide melts, and R values from Hiebert et al. (2016)*
[3] *This study*
[4] *Modified from Ripley and Li 2003*
[5] *From Faure 1998*
[6] *From Liu et al. 2018*

Highlights

- Large Ni isotopic fractionation with unknown cause has been observed in komatiites
- Fractionation occurs in two stages
- Fractionation during isotopic exchange between komatiite and sulfide liquids
- Rayleigh fractionation during crystallization of sulfide liquid

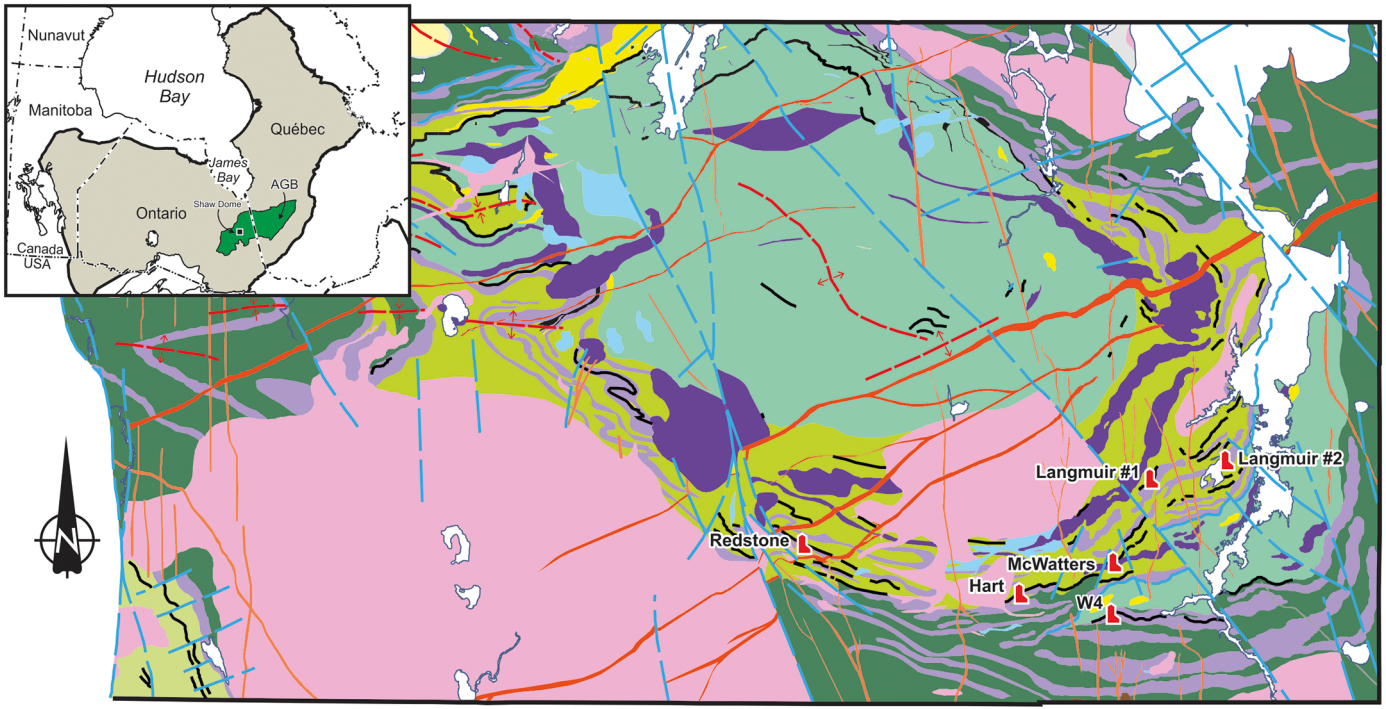
Nunavut
Hudson Bay
Manitoba
Québec
James Bay
AGB
Ontario
Shaw Dome
Canada
USA
N
Redstone
Langmuir #1
Langmuir #2
McWatters
Hart
W4
PRECAMBRIAN
Mafic Intrusive Rocks
Mafic Intrusive Rocks
ARCHEAN
Felsic to Intermediate Intrusive Rocks
Mafic Intrusive Rocks
2692-2669 Ma (Timiskaming)
Intermediate Metavolcanic and/or Epiclastic Rocks
2707-2682 Ma (Porcupine)
Clastic Metasedimentary Rocks
Felsic Metavolcanic Rocks
2710-2704 Ma Volcanic Episode (Tisdale)
Komatiitic Ultramafic Metavolcanic Rocks
Komatiitic Ultramafic Intrusive Rocks
Chemical Metasedimentary Rocks
Intermediate to Felsic Metavolcanic Rocks
Mafic Metavolcanic Rocks
2734-2724 Ma Volcanic Episode (Deloro)
Intermediate to Felsic Metavolcanic Rocks
Chemical Metasedimentary Rocks
Intermediate to Mafic Metavolcanic Rocks
Anticline, syncline
Faults
Komatiite-Associated Ni-Cu-(PGE) Mineralization
Past Producers/Deposits
0
10
Kilometres

Figure 1

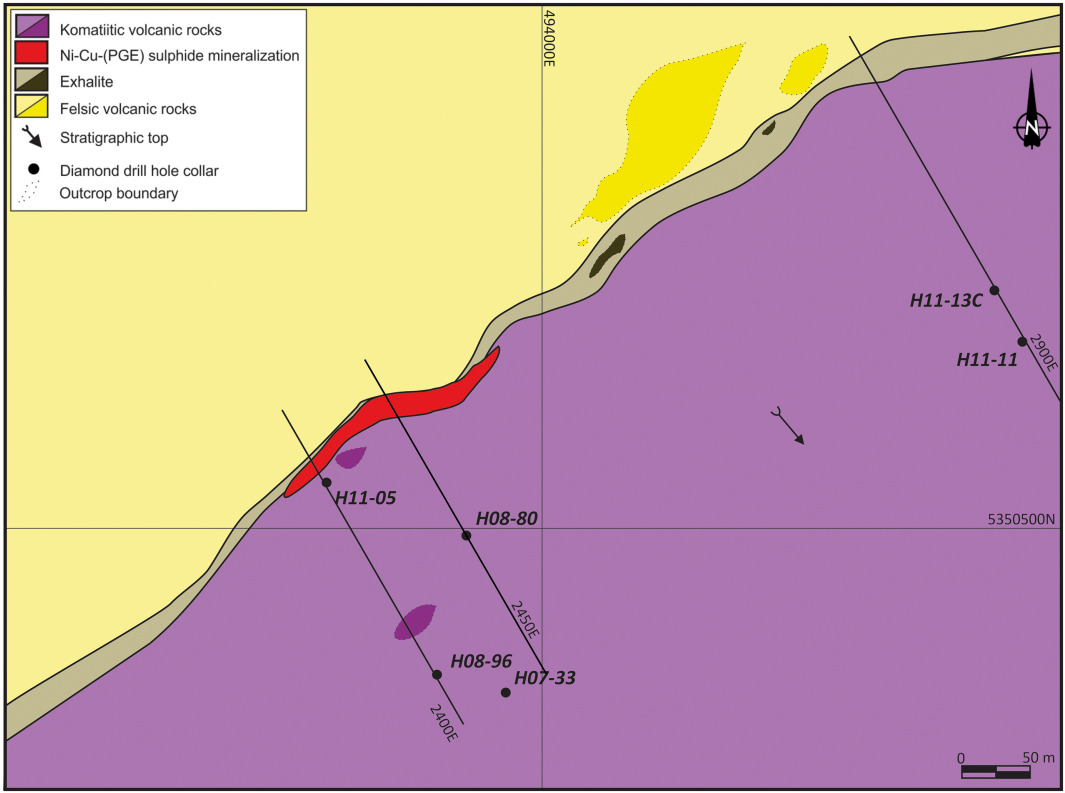
Komatiitic volcanic rocks
Ni-Cu-(PGE) sulphide mineralization
Exhalite
Felsic volcanic rocks
Stratigraphic top
Diamond drill hole collar
Outcrop boundary
494000E
N
H11-13C
H11-11
2900E
H11-05
H08-80
5350500N
2450E
H08-96
H07-33
2400E
0
50 m

Figure 2

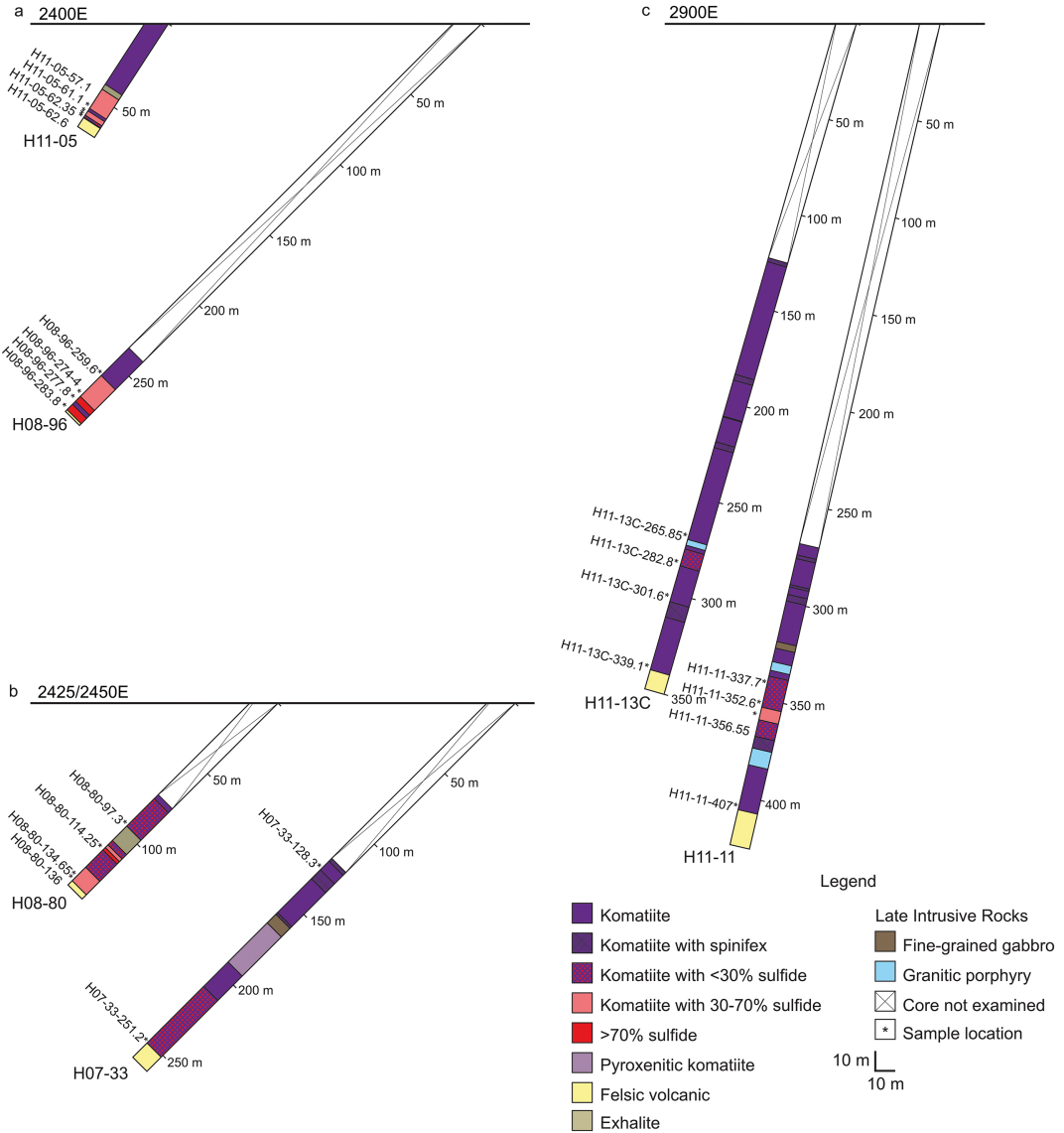
a
2400E
H11-05-57.1
H11-05-61.1*
H11-05-62.35*
H11-05-62.6
50 m
H11-05
50 m
100 m
150 m
200 m
H08-96-259.6*
H08-96-274.4*
H08-96-277.8*
H08-96-283.8*
250 m
H08-96
b
2425/2450E
50 m
H08-80-97.3*
H08-80-114.25*
H08-80-134.65*
H08-80-138*
100 m
H08-80
50 m
H07-33-128.3*
100 m
150 m
200 m
H07-33-251.2*
250 m
H07-33
c
2900E
50 m
50 m
100 m
100 m
150 m
150 m
200 m
200 m
250 m
250 m
H11-13C-265.85*
H11-13C-282.8*
H11-13C-301.6*
300 m
300 m
H11-13C-339.1*
H11-11-337.7*
H11-11-352.6*
350 m
350 m
H11-11-356.55*
H11-13C
H11-11-407*
400 m
H11-11
Legend
Komatiite
Komatiite with spinifex
Komatiite with <30% sulfide
Komatiite with 30-70% sulfide
>70% sulfide
Pyroxenitic komatiite
Felsic volcanic
Exhalite
Late Intrusive Rocks
Fine-grained gabbro
Granitic porphyry
Core not examined
Sample location
10 m
10 m

Figure 3

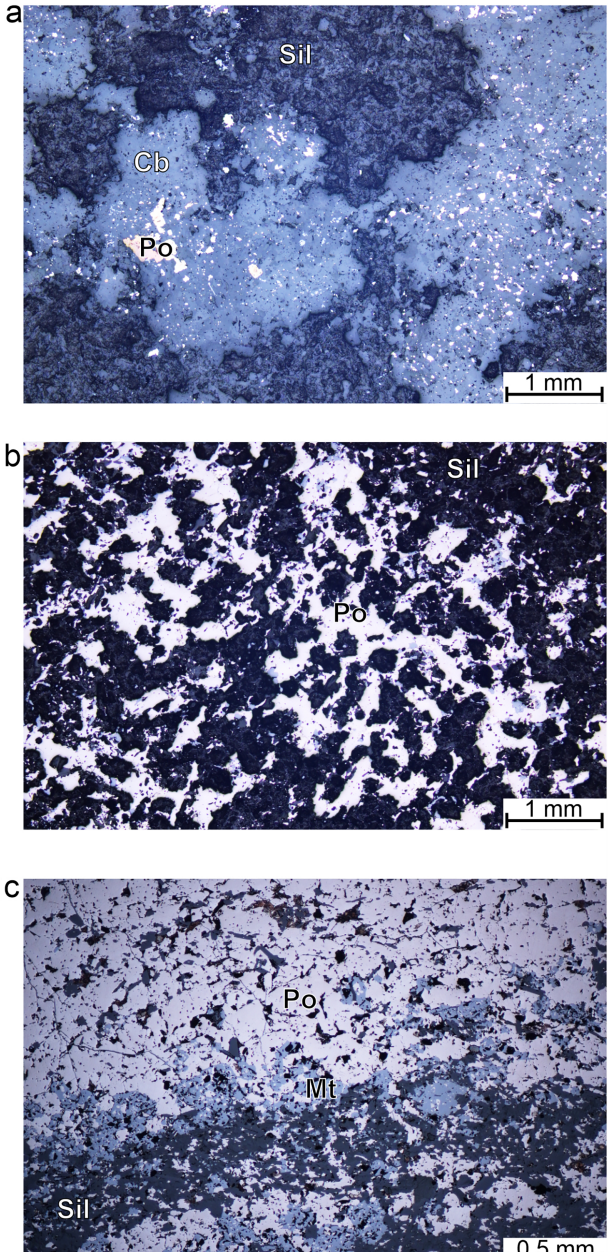

Figure 4

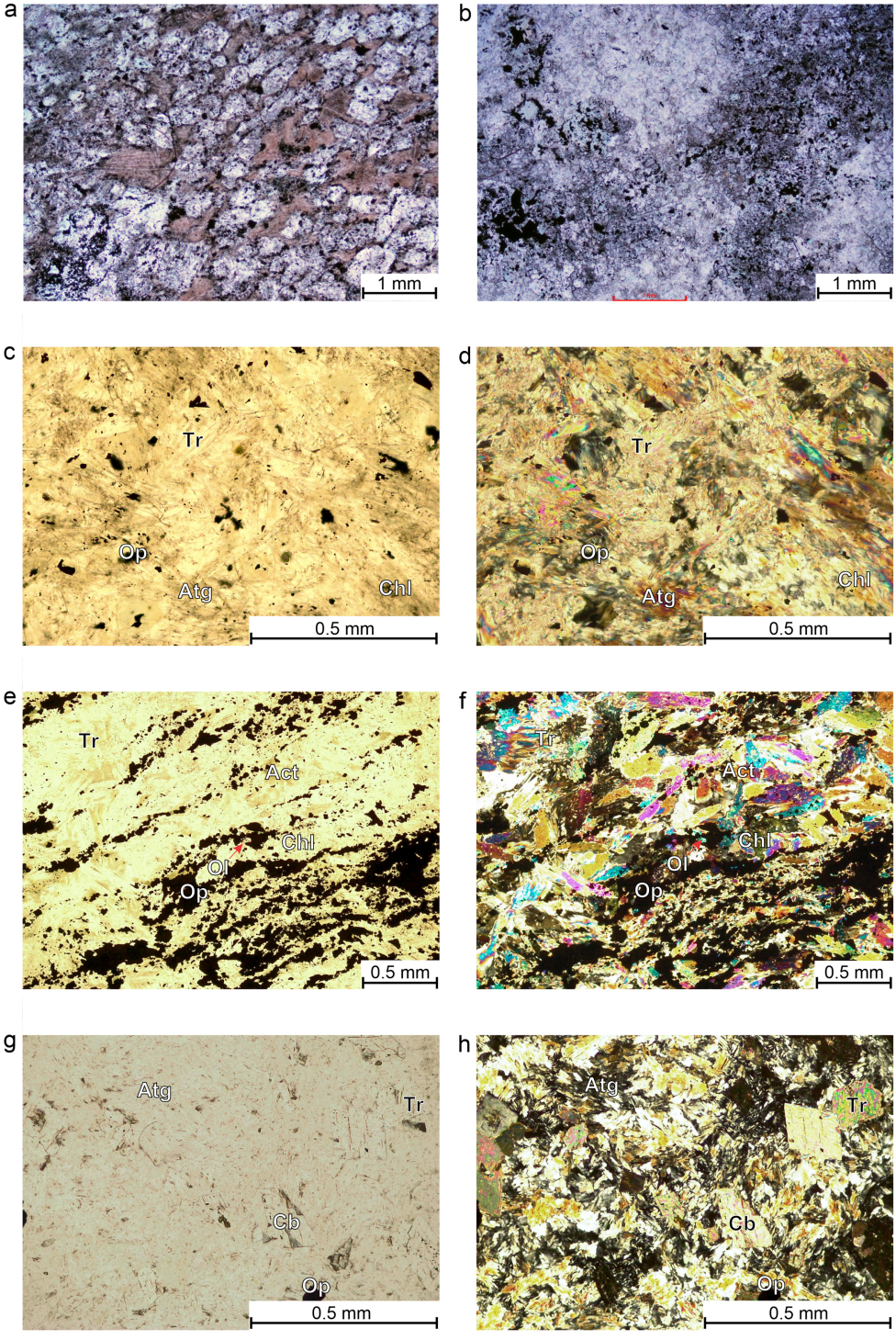
a
1 mm
b
1 mm
c
Tr
Op
Atg
Chl
0.5 mm
d
Tr
Op
Atg
Chl
0.5 mm
e
Tr
Act
Chl
Ol
Op
0.5 mm
f
Tr
Act
Chl
Ol
Op
0.5 mm
g
Atg
Tr
Cb
Op
0.5 mm
h
Atg
Tr
Cb
Op
0.5 mm

Figure 5

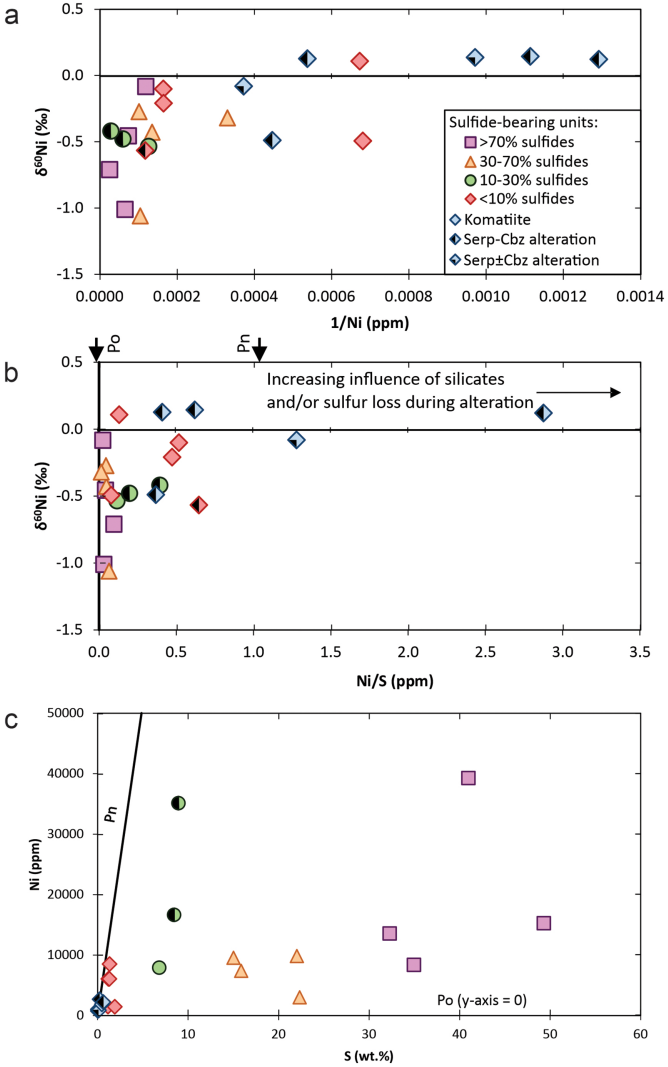
a
δ60Ni (‰)
1/Ni (ppm)
Sulfide-bearing units:
>70% sulfides
30-70% sulfides
10-30% sulfides
<10% sulfides
Komatiite
Serp-Cbz alteration
Serp±Cbz alteration
b
Po
Pn
Increasing influence of silicates
and/or sulfur loss during alteration
δ60Ni (‰)
Ni/S (ppm)
c
Ni (ppm)
Pn
Po (y-axis = 0)
S (wt.%)

Figure 6

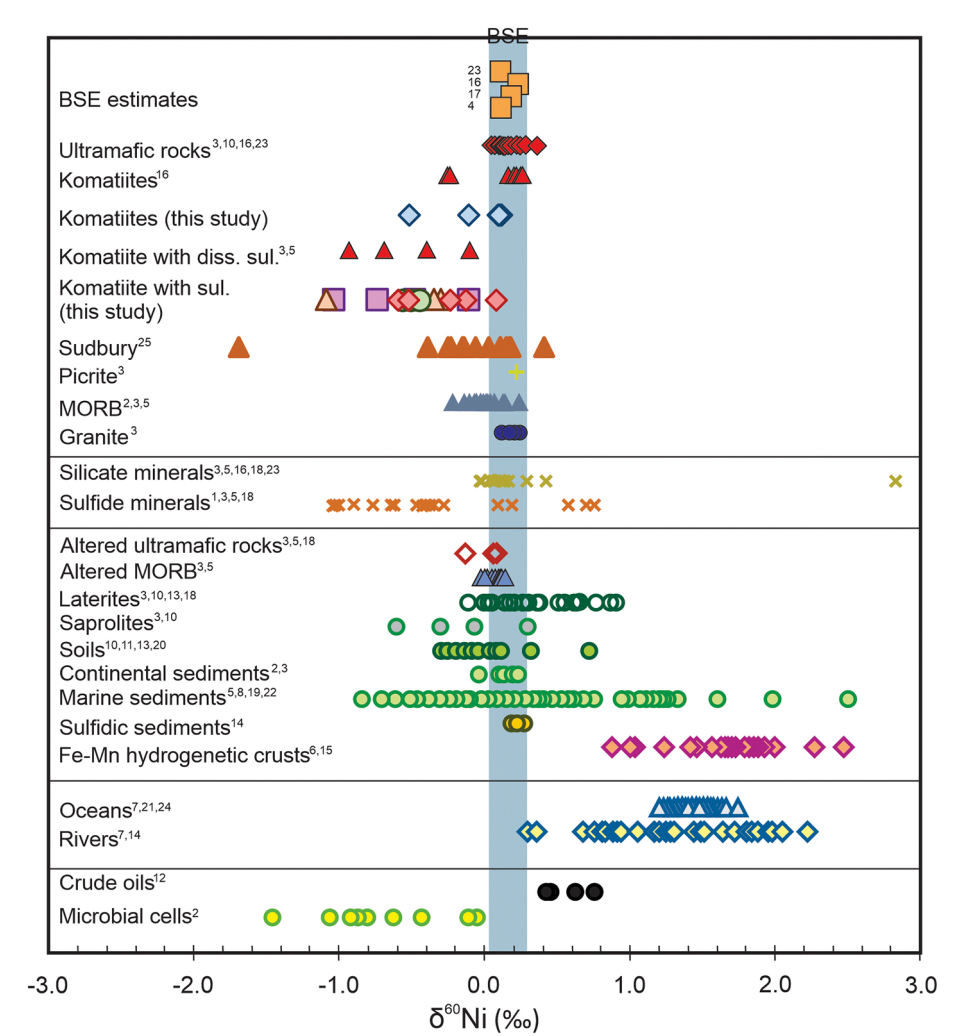
BSE
BSE estimates
23
16
17
4
Ultramafic rocks[3,10,16,23]
Komatiites[16]
Komatiites (this study)
Komatiite with diss. sul.[3,5]
Komatiite with sul. (this study)
Sudbury[25]
Picrite[3]
MORB[2,3,5]
Granite[3]
Silicate minerals[3,5,16,18,23]
Sulfide minerals[1,3,5,18]
Altered ultramafic rocks[3,5,18]
Altered MORB[3,5]
Laterites[3,10,13,18]
Saprolites[3,10]
Soils[10,11,13,20]
Continental sediments[2,3]
Marine sediments[5,8,19,22]
Sulfidic sediments[14]
Fe-Mn hydrogenetic crusts[6,15]
Oceans[7,21,24]
Rivers[7,14]
Crude oils[12]
Microbial cells[2]
-3.0
-2.0
-1.0
0.0
1.0
2.0
3.0
δ60Ni (‰)

Figure 7

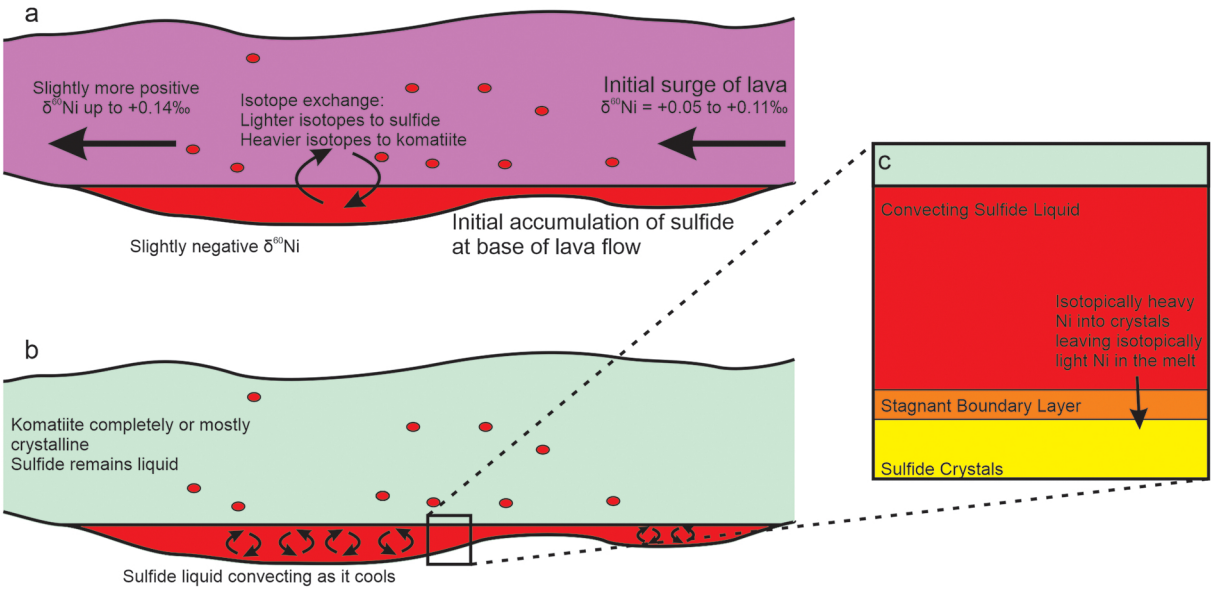
a
Slightly more positive
δ60Ni up to +0.14‰
Isotope exchange:
Lighter isotopes to sulfide
Heavier isotopes to komatiite
Initial surge of lava
δ60Ni = +0.05 to +0.11‰
Slightly negative δ60Ni
Initial accumulation of sulfide
at base of lava flow
b
Komatiite completely or mostly
crystalline
Sulfide remains liquid
Sulfide liquid convecting as it cools
c
Convecting Sulfide Liquid
Isotopically heavy
Ni into crystals
leaving isotopically
light Ni in the melt
Stagnant Boundary Layer
Sulfide Crystals

Figure 8

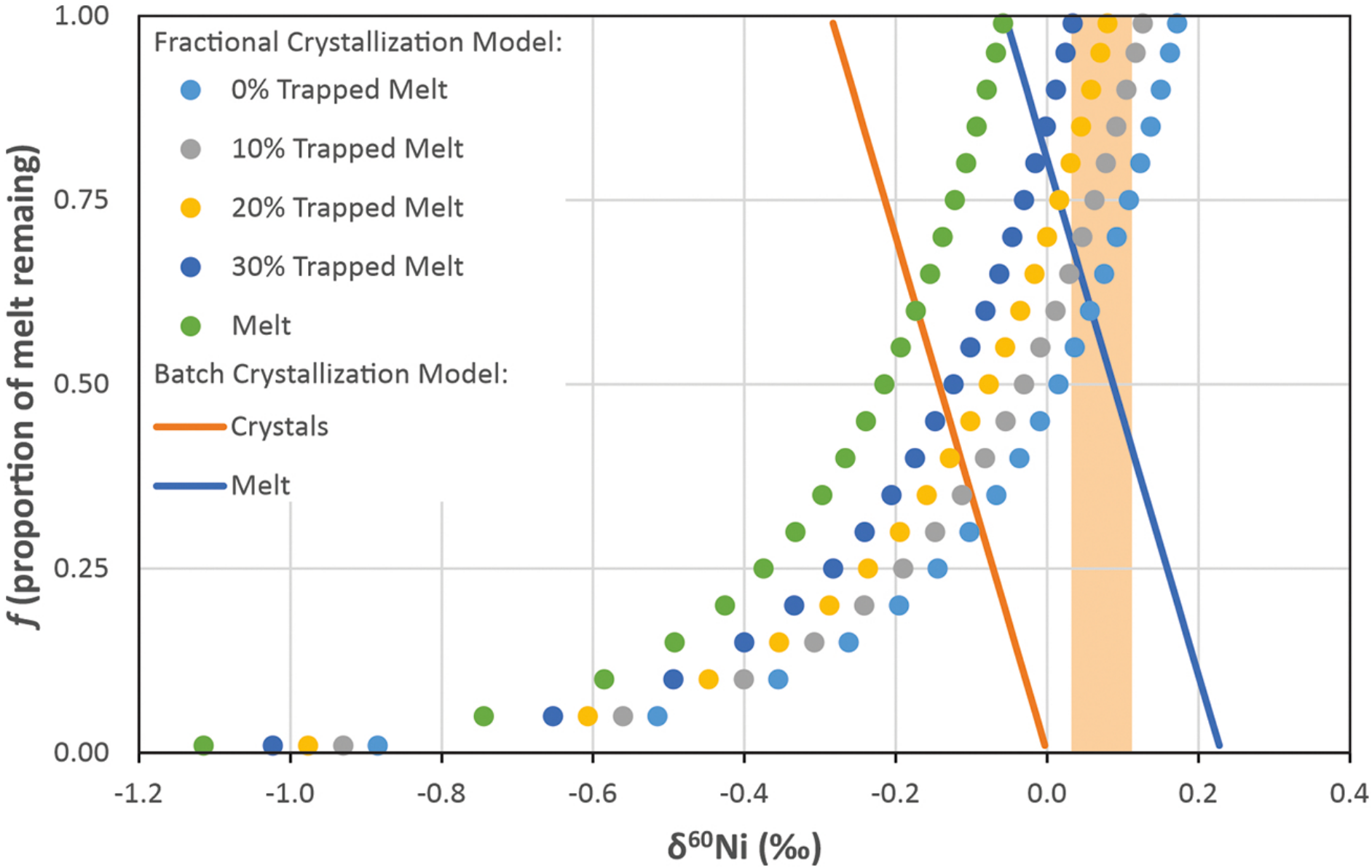
Fractional Crystallization Model:
0% Trapped Melt
10% Trapped Melt
20% Trapped Melt
30% Trapped Melt
Melt
Batch Crystallization Model:
Crystals
Melt
f (proportion of melt remaing)
1.00
0.75
0.50
0.25
0.00
-1.2
-1.0
-0.8
-0.6
-0.4
-0.2
0.0
0.2
0.4
δ60Ni (‰)

Figure 9

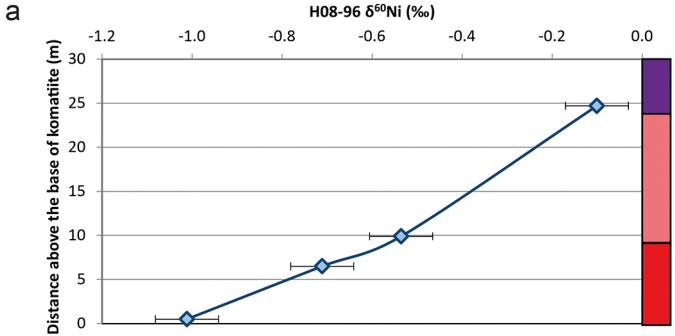
a
H08-96 δ60Ni (‰)
-1.2
-1.0
-0.8
-0.6
-0.4
-0.2
0.0
Distance above the base of komatiite (m)
0
5
10
15
20
25
30

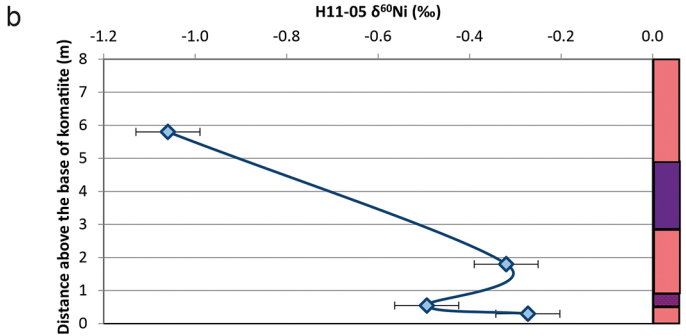
b
H11-05 δ60Ni (‰)
-1.2
-1.0
-0.8
-0.6
-0.4
-0.2
0.0
Distance above the base of komatiite (m)
0
1
2
3
4
5
6
7
8

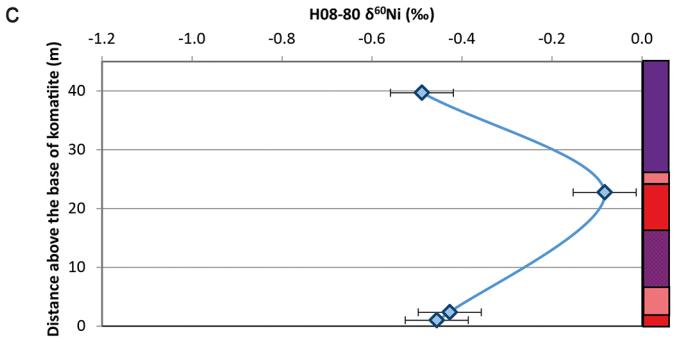
c
H08-80 δ60Ni (‰)
-1.2
-1.0
-0.8
-0.6
-0.4
-0.2
0.0
Distance above the base of komatiite (m)
0
10
20
30
40

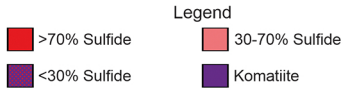
Legend
>70% Sulfide
30-70% Sulfide
<30% Sulfide
Komatiite

Figure 10